1-1-2012

Rapid microwave-assisted synthesis of Mn3O4-graphene nanocomposite and its lithium storage properties

Li Li
University of Wollongong, li@uow.edu.au

Zaiping Guo
University of Wollongong, zguo@uow.edu.au

Aijun Du
University of Queensland

Hua-Kun Liu
University of Wollongong, hua@uow.edu.au

Journal of Materials Chemistry

Cite this: J. Mater. Chem., 2012, 22, 3600

www.rsc.org/materials

PAPER

Rapid microwave-assisted synthesis of Mn_3O_4–graphene nanocomposite and its lithium storage properties†

Li Li,[a] Zaiping Guo,*[ab] Aijun Du*[c] and Huakun Liu[a]

Received 8th October 2011, Accepted 9th December 2011
DOI: 10.1039/c2jm15075a

A nanocomposite of Mn_3O_4 wrapped in graphene sheets (GSs) was successfully synthesized *via* a facile, effective, energy-saving, and scalable microwave hydrothermal technique. The morphology and microstructures of the fabricated GS–Mn_3O_4 nanocomposite were characterized using various techniques. The results indicate that the particle size of the Mn_3O_4 particles in the nanocomposite markedly decreased to nearly 20 nm, significantly smaller than that for the bare Mn_3O_4. Electrochemical measurements demonstrated a high specific capacity of more than 900 mA h g^{-1} at 40 mA g^{-1}, and excellent cycling stability with no capacity decay can be observed up to 50 cycles. All of these properties are also interpreted by experimental studies and theoretical calculations.

1 Introduction

Manganese oxide, due to its low toxicity and natural abundance, as well as its low price, has been a key topic among the transition-metal oxides. Besides its potential applications in diverse areas, including catalysis[1–3] and electrochromic applications,[4a] its suitability for rechargeable lithium ion batteries (LIBs),[4b] as well as high power supercapacitors,[5] has also attracted worldwide interest in the energy storage field. The theoretical specific capacity of Mn_3O_4 is around 937 mA h g^{-1}, which is nearly three times higher than that of graphite (~372 mA h g^{-1}). Nevertheless, only a few papers have reported Mn_3O_4 in lithium batteries so far, as it is virtually an insulator with very low electrical conductivity (~10^{-7} to 10^{-8} S cm^{-1}), which limits its capacity to around 400 mA h g^{-1}, even with the addition of cobalt.[6] Graphene, as a rising star in materials science with its well-defined two-dimensional honeycomb-like network of carbon atoms, has aroused explosive interest in the nanoscience and nanotechnology fields owing to its outstanding thermal stability,[7] superior electronic conductivity (~2000 S cm^{-1}),[8] large theoretical specific surface area (~2630 m^2 g^{-1}), and high intrinsic mobility (200 000 cm^2 V^{-1} s^{-1}),[9,10] as well as its remarkable structural flexibility.[11,12] Therefore, in light of its fascinating merits and low costs, it has been suggested that graphene sheet (GS) could be an ideal substrate for growth of functional nanomaterials[13–15] to render them electrochemically active and electrically conductive. With this in mind, numerous graphene-based inorganic nanocomposites with metal,[16–19] metal oxides,[20–24] and sulfide[14] have been successfully synthesized and show enhanced properties of these host materials.

Herein, we have employed a novel, facile, and fast one-pot microwave hydrothermal technique to obtain well-organized Mn_3O_4 encapsulated in graphene sheets (GS–Mn_3O_4). Compared with the traditional hydrothermal method, the microwave hydrothermal method can increase the kinetics of crystallization by causing rapid nucleation and growth, which can dramatically reduce the reaction time from 10 hours[25] or even several days *via* the conventional hydrothermal method down to 30 min, as reported here, and therefore it can save a large amount of energy. Additionally, the most important point to be noted is that, compared with the conventional hydrothermal method, the application of microwaves in the heating process offers a great possibility for large-scale batch reactions. Furthermore, through the microwave hydrothermal method, various multifunctional nanomaterials with intriguing morphologies, such as nanospheres, nanowires, and nanoporous networks, can be produced effectively and efficiently.[26–28]

Through this rapid and robust *in situ* approach, the microwave hydrothermal technique, a hierarchical nanocomposite of Mn_3O_4 embedded in graphene sheets (GS–Mn_3O_4) was synthesized directly from graphite oxide (GO) and manganese acetate in the presence of anhydrous hydrazine. The reduction of GO and the loading of Mn_3O_4 nanoparticles on the graphene sheets occurred simultaneously, which can avoid the introduction of additional molecular cross-linkers to bridge the nanoparticles and the graphene matrix. Therefore, the graphene sheets in the composite can not only efficiently buffer the volume change of

[a]*Institute for Superconducting and Electronics Materials, University of Wollongong, Wollongong, 2500, Australia. E-mail: zguo@uow.edu.au; Fax: +61 2 42215225*
[b]*School of Mechanical, Materials, and Mechatronic Engineering, University of Wollongong, Wollongong, 2500, Australia*
[c]*Centre for Computational Molecular Science, Australian Institute for Bioengineering and Nanotechnology and School of Chemical Engineering, University of Queensland, Queensland, 4072, Australia. E-mail: a.du@uq.edu.qu*

† Electronic supplementary information (ESI) available: TGA curves, CV curves, computational details and Nyquist plots. See DOI: 10.1039/c2jm15075a

Mn_3O_4 nanoparticles during charging and discharging processes but also preserve the high electrical conductivity of the whole electrode. As a consequence, the fabricated GS–Mn_3O_4 hybrid material possesses high reversible capacity, good cycle life, and high rate capability as anode material for lithium ion batteries, and hence could be considered as a candidate electrode material for high-performance energy storage devices.

2 Experimental section

2.1 Synthesis of the GS–Mn_3O_4 nanocomposite

Graphite oxide was prepared using a modified Hummers' method as described elsewhere.[29] In a typical preparation of GS–Mn_3O_4 nanocomposite, 20 mL of GO (0.5 mg mL^{-1}) suspension was diluted to 100 mL solution by adding 80 mL deionized water, followed by stirring for 0.5 h. Then, 10 mL of manganese acetate aqueous solution (0.2 M) was added into the as-prepared GO dispersion under vigorous magnetic stirring for 4 hours, and 2 mL of NaOH aqueous solution (2 M) was added dropwise to the above mixture, followed by stirring overnight. Subsequently, 0.2 mL hydrazine anhydrous was added to the above solution with stirring for 0.5 h, and then the solution was diluted by addition of 100 mL deionized water. Finally, 20 mL of the resultant brown solution was transferred to a Teflon-lined autoclave and then was irradiated by microwaves for 30 min at 150 °C at a fast heating rate. Please note that the temperature we used is lower and the process is much faster than that reported recently.[25] After the reaction, the precipitate was collected with a centrifuge and rinsed with deionized water and ethanol three times, respectively. Afterwards, the obtained powders were dried at 60 °C overnight in a vacuum oven. For comparison, bare Mn_3O_4 nanoparticles were also prepared by the same experimental procedures but without adding graphite oxide. By using this method, it was estimated from thermogravimetric analysis (TGA) that the amount of graphene in the GS–Mn_3O_4 nanocomposite was about 18.8 wt%, as shown in Fig. S1 in the ESI†.

2.2 Materials characterization

The phase structures and molecules of the as-prepared products were characterized by MMA GBC X-ray diffraction with Cu Kα radiation and Raman spectroscopy (Jobin Yvon HR800). The morphology and size of the as-obtained products were investigated using a field-emission scanning electron microscope (FESEM; JEOL-7500, 2 keV) and a transmission electron microscope (TEM, JEOL 2011, 200 keV). Thermogravimetric analysis was conducted on a TA 2000 Thermoanalyzer. The working electrodes were prepared by mixing the as-prepared samples, carbon black (Super P, MMM, Belgium), and poly (vinyl difluoride) (PVDF) in a weight ratio of 8 : 1 : 1. The resultant slurry was pasted on Cu foil and dried in a vacuum oven at 80 °C for 8 h. The electrochemical measurements were carried out in CR2032 coin cells with Li foil as the counter electrode and 1 M $LiPF_6$ in 1 : 1 ethylene carbonate (EC) and dimethyl carbonate (DMC) as the electrolyte. Cyclic voltammograms were collected on a VMP-3 electrochemical workstation at a scan rate of 0.1 mV s^{-1}. The discharge and charge measurements were conducted on a Land CT2001A battery tester.

3 Results and discussion

Fig. 1 presents the X-ray diffraction (XRD) patterns of graphene, graphite oxide (GO), and bare Mn_3O_4 nanoparticles, as well as the as-prepared GS–Mn_3O_4 nanocomposite, respectively. The diffraction peak at 9.7° is indexed to GO in Fig. 1(b), and the appearance of the (002) diffraction line at 23.4° for graphene[30] in Fig. 1(a) gives evidence that the graphite oxide was reduced to graphene during the microwave hydrothermal process. Meanwhile, it can also be observed that the graphene peaks become broadened after the reduction, which is a typical pattern of amorphous carbon structure,[31] revealing that the stacking of GS is substantially disordered.

The characteristic peaks, as labelled in Fig. 1(c) and (d), of the crystal structure of Mn_3O_4 in both the nanoparticles and the nanocomposite are in good agreement with tetragonal spinel with space group *I*41/*amd* (JCPDS card: 24-0734), which also matches well with previous reports in the literature,[25] and no other impure crystalline phases were observed. The peaks of the GS–Mn_3O_4 nanocomposite become broadened compared with those of bare Mn_3O_4, indicating that the grain size of the Mn_3O_4 nanoparticles is smaller in the presence of the GS encapsulation than for the bare Mn_3O_4.

In addition, the presence of both graphene and Mn_3O_4 can be confirmed from typical peaks in the Raman spectra (Fig. 2). Raman scattering probes the vibration modes of both crystalline and amorphous materials, providing complementary structural information to X-ray diffraction. Fig. 2 presents the Raman spectra of GO, GS–Mn_3O_4 composite, and bare Mn_3O_4 nanoparticles. For the GO and GS–Mn_3O_4 samples, the G band (1604 cm^{-1}) arises from the zone centre E_{2g} mode, corresponding to ordered sp^2 bonded carbon, whereas the D band (1330 cm^{-1}) is ascribed to edges or disordered layers. The intensity ratio of the D to the G band (I_D/I_G) provides a sensitive measure of the disorder and crystallite size of the graphitic layers.[32] The intensity ratio (1.08) of I_D/I_G for GO is lower than that (1.31) of GS–Mn_3O_4 composite, suggesting that the reduction of exfoliated

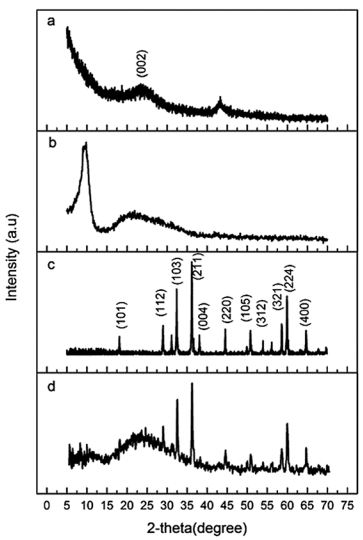

Fig. 1 X-Ray diffraction patterns of (a) graphene, (b) GO, (c) bare Mn_3O_4, and (d) as-prepared GS–Mn_3O_4 nanocomposite.

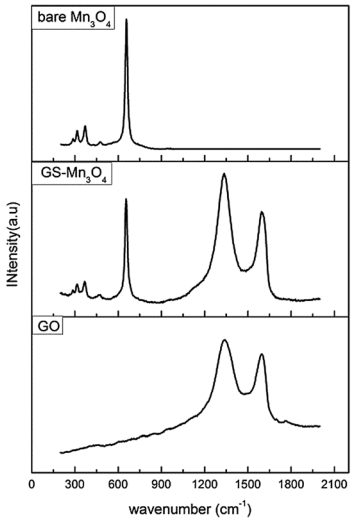

Fig. 2 Raman spectra of bare Mn_3O_4 nanoparticles, GS–Mn_3O_4 nanocomposite, and GO.

GO leads to smaller and more disordered layers, as well as dramatically decreasing the layer numbers of graphene.[33] In addition, minor peaks at 317, 374, and 475 cm^{-1} and a dominant peak at 652 cm^{-1} in the GS–Mn_3O_4 nanocomposite can be ascribed to crystalline Mn_3O_4,[34,35] which is substantially coincident with the bare Mn_3O_4. The Raman spectrum of the GS–Mn_3O_4 nanocomposite is actually that of a combination of pure graphene and bare Mn_3O_4. This implies that Mn_3O_4 and GS are all in their own pristine structure, and no reactions have occurred between them during the *in situ* microwave hydrothermal synthesis process.

To investigate the morphology of the products, field-emission scanning electron microscope (FESEM) images were collected for the bare Mn_3O_4 nanoparticles and the GS–Mn_3O_4 nanocomposite, as shown in Fig. 3. The morphology of the bare Mn_3O_4 nanoparticles, prepared by the same procedure, but in the absence of GO, is spherical, but the nanoparticles are severely aggregated together, giving rise to a bigger particle size in the range of 40–100 nm (Fig. 3(a)). In comparison, we can observe that the size of the Mn_3O_4 nanoparticles is dramatically decreased to around 20 nm when they are prepared *in situ* with graphene *via* the microwave hydrothermal method, as shown in Fig. 3(b). This is because intimate interaction between bare Mn_3O_4 particles and hierarchic flexible graphene sheets drastically limits the growth and limits the agglomeration of the crystalline Mn_3O_4 particles to some extent, while the Mn_3O_4 particles are encapsulated in a matrix of graphene sheets, leading to more effective ionic and electron transport during Li^+ insertion/de-insertion due to the high conductivity of graphene.

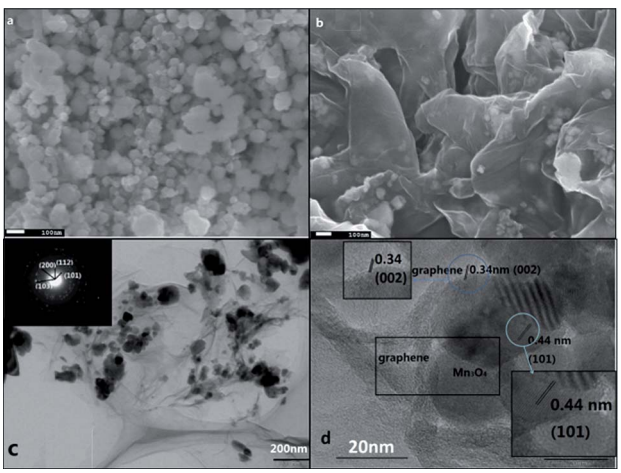

Fig. 3 FESEM images of (a) bare Mn_3O_4 nanoparticles and (b) GS–Mn_3O_4 nanocomposite. TEM images of the GS–Mn_3O_4 nanocomposite: (c) large-area image and associated SAED pattern (inset), (d) high-resolution TEM image of the Mn_3O_4 particle in [101] orientation embedded in graphene sheets and associated selected-area magnified images (insets).

The transmission electron microscope (TEM) images shown in Fig. 3(c) and (d) reveal that the Mn_3O_4 nanoparticles were distributed on the surface of the graphene nanosheets in the form of single particles or small particle clusters, and the nature of the Mn_3O_4 particles shown in Fig. 3(c) was further confirmed by selected area electron diffraction (SAED) patterns (inset of Fig. 3(c)). These visible diffraction rings can be indexed to the Hausmannite Mn_3O_4 phase, which is consistent with the XRD patterns. The high-resolution TEM image (Fig. 3(d)) indicates that there are multiple overlapping layers near the edge of the Mn_3O_4 particle, whereas the *d*-spacing of the (002) graphene planes is 0.34 nm, almost equal to the value of pristine graphene. The Mn_3O_4 particles were firmly encapsulated by the graphene sheets, and the crystal lattice fringes with *d*-spacing of 0.44 nm can be assigned to the [101] plane of tetragonal Mn_3O_4. Based on the TEM images, it could be further confirmed that there is an intimate interaction between the Mn_3O_4 particles and the graphene sheets, and such a combination can enable fast electron transport through the graphene matrix to the Mn_3O_4 nanoparticles, guaranteeing efficient electrochemical performance.

In order to highlight the superiority of the GS–Mn_3O_4 nanocomposite as anode material in LIBs, the discharge/charge profiles of the GS–Mn_3O_4 nanocomposite and the bare Mn_3O_4 nanoparticles at a current density of 40 mA g^{-1} are displayed in Fig. 4(a) and (b), respectively. The cyclic voltammetry (CV) curves of the GS–Mn_3O_4 nanocomposite and the bare Mn_3O_4 nanoparticles at a scan rate of 0.1 mV s^{-1} in the potential range from 0.1 V to 3 V are shown in Fig. S2 in the ESI†. The general features of the discharge/charge profiles are consistent with those of other transition metal oxides such as Co, Fe, and Ni oxide as anode materials in LIBs, but their mechanism of Li reactivity differs from the classical Li insertion/de-insertion or Li-alloying processes, which involves the formation and decomposition of Li_2O and accompanying reduction and oxidation of metal nanoparticles, as reported by P. Poizot *et al.*[36]

As can be seen from Fig. 4(a), there is an obvious sloping part in the first discharge cycle from 1.5 V to 0.38 V, consistent with two broad cathodic peaks at around 0.62 V and 1.26 V, as shown in Fig. S2(a)†, which can be ascribed to the decomposition of the electrolyte solvent and the formation of the solid electrolyte interphase, as well as initial reduction of Mn_3O_4. We can also observe that a well-defined voltage plateau is present at around 0.38 V in the first discharge cycle as shown in Fig. 4(a), which can be attributed to the further reduction of MnO to Mn and the

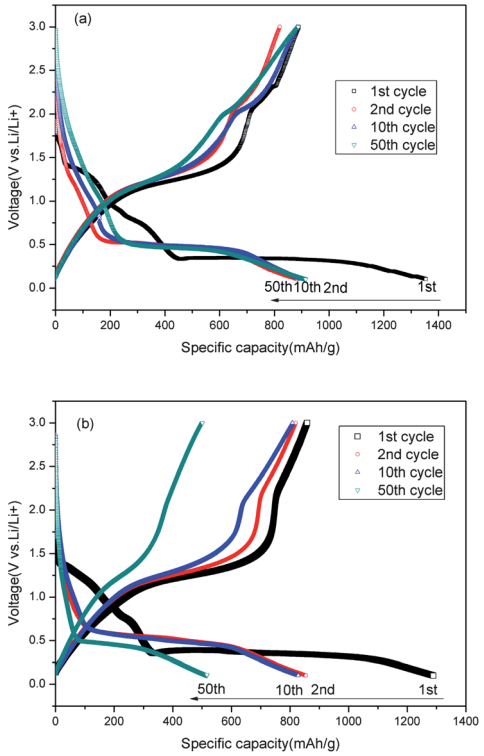

Fig. 4 Galvanostatic charge/discharge profiles for selected cycles of (a) GS–Mn_3O_4 nanocomposite, and (b) bare Mn_3O_4 nanoparticles at the current density of 40 mA g^{-1} with the potential window from 0.1 V to 3 V.

formation of amorphous Li_2O ($Mn_3O_4 + 8Li^+ + 8e^- = 3Mn + 4Li_2O$), while the capacity extends to approximately 1354 mA h g^{-1}, slightly higher than the theoretical capacity of 937 mA h g^{-1} for the conversion reaction to Mn and Li_2O.[36,37] The higher capacity in the first cycle should be ascribed to the following factors: the discharge capacity in the first cycle is not only contributed by the conversion reaction of Mn_3O_4 to Mn nanoparticles, along with the formation of amorphous Li_2O, but also corresponds to the formation of the solid electrolyte interphase (SEI), which is not included in the theoretical capacity of Mn_3O_4. Therefore, the initial discharge capacity is higher than the theoretical value. This is a normal phenomenon in metal oxide anode materials for lithium storage.

At the same time, an apparent broad peak at around 1.34 V in the first cycle is recorded in the anodic process as shown in Fig. S2(a)†, corresponding to the reversible oxidation of Mn(0) to MnO during the anodic process. An additional shoulder peak is observed when the material is charged above 2 V; this may correspond to further oxidation of MnO to Mn_3O_4, since it cannot be observed in the charge curve of MnO.[37] The first charge capacity approaches 890 mA h g^{-1} as shown in Fig. 4(a), which is very close to the theoretical capacity (937 mA h g^{-1}) of a fully reversible conversion reaction. In the subsequent cycles, as shown in Fig. S2(a)†, the reduction peaks in the first cycle have disappeared, and a new sharp peak near 0.31 V appears instead, reflecting the sloping voltage range from 0.6 V to 0.1 V in the second cycle of the charge/discharge curve, as shown in Fig. 4(c), which is distinctly higher than for the first discharge, indicating that the lithium insertion reaction in the second cycle has become easier. Fig. 4(b) presents discharge/charge profiles of the bare Mn_3O_4 nanoparticles, which are similar to the curve shapes for the GS–Mn_3O_4 nanocomposite, except for the relatively poor cycling performance.

The cycling performances of the GS–Mn_3O_4 nanocomposite and the bare Mn_3O_4 nanoparticles were measured at a current density of 40 mA g^{-1} in the voltage range from 0.1 V to 3 V, and the results are shown in Fig. 5(a). We can observe that the second discharge specific capacity of the bare Mn_3O_4 (854.6 mA h g^{-1}) is very close to that of the GS–Mn_3O_4 nanocomposite (901.3 mA h g^{-1}), however, it declines dramatically to only 496 mA h g^{-1} after 50 cycles, *i.e.*, 58% of the capacity in the second cycle. In contrast, the GS–Mn_3O_4 nanocomposite maintains a significantly higher reversibility, and it is interesting to note that its reversible capacity even gradually increases to 927 mA h g^{-1} at the 20th cycle, which is well-documented in the literature and is attributed to the reversible growth of a polymeric gel-like film resulting from kinetically activated electrolyte degradation.[38–40] The coulombic efficiency of the GS–Mn_3O_4 composite after the second cycle remains nearly 100% up to 50 cycles. We have also compared the rate performance of the GS–Mn_3O_4 nanocomposite with that of the bare Mn_3O_4 at different current densities of 40, 100, 200, 500, 1000, and 2000 mA g^{-1}, shown in Fig. 5(b). At 1000 mA g^{-1}, the reversible capacity of the GS–Mn_3O_4 nanocomposite reaches over 400 mA h g^{-1}, while the capacity of the bare Mn_3O_4 is less than 250 mA h g^{-1}. Remarkably, when the current density is again reduced back to 40 mA g^{-1}, the stable capacity of the GS–Mn_3O_4 nanocomposite can be almost resumed, and the discharge specific capacity is even slightly

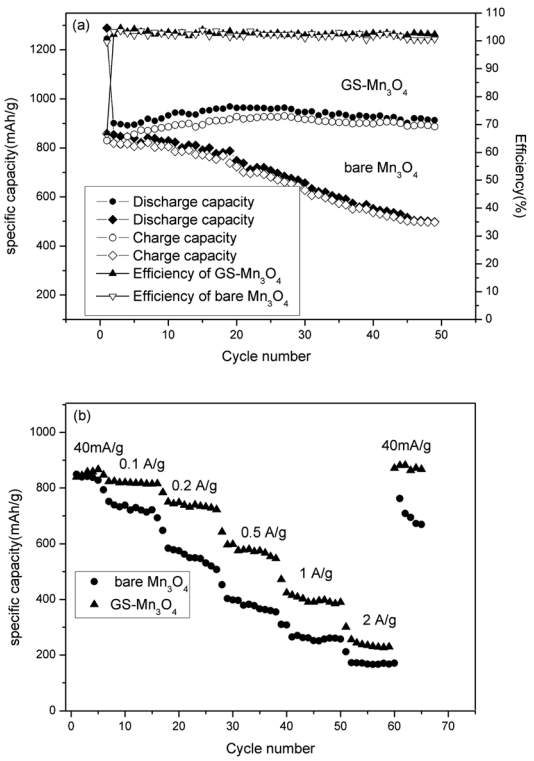

Fig. 5 (a) Cycling performance of the GS–Mn_3O_4 nanocomposite and bare Mn_3O_4 at a current density of 40 mA g^{-1}; (b) rate performance of GS–Mn_3O_4 nanocomposite and bare Mn_3O_4 particles at different current densities.

higher than that before at 40 mA g^{-1}, indicating excellent cycling stability.

From the comparison between the GS–Mn_3O_4 nanocomposite and the bare Mn_3O_4, we can conclude that the excellent electrochemical performance, including high reversible capacity, improved cycle stability, and high rate performance, of the GS–Mn_3O_4 nanocomposite can be ascribed to the following factors: first, the high conductivity of the graphene sheets plays a significant role, as the GS acts as an ionic and electronic transport medium in the electrode during the charge/discharge processes; secondly, the decreased particle size of Mn_3O_4 particles in the composite material and the intimate interaction between the flexible GS and the Mn_3O_4 particles directly fabricated on the surface of the GS not only effectively confines the growth of the Mn_3O_4 particles, but also affords an elastic buffer to alleviate the agglomeration and cracking of Mn_3O_4 particles that is associated with the volume expansion during cycling, thus maintaining the structural integrity and avoiding rapid loss of electrode capacity, which is beneficial for cycling stability, and also enables Li ion transport from Mn_3O_4 particles to be more effective and rapid. Hence, such a nanocomposite could deliver an enhanced electrochemical performance as an anode material in rechargeable LIBs.

To gain further understanding of the relationship between the graphene sheets and the bare Mn_3O_4 nanoparticles, we conducted a series of calculations (see computational details in the ESI†) to study the charge transfer from the graphene layer to Mn_3O_4. Fig. 6(a) exhibits a top view of the fully relaxed GS–Mn_3O_4(001) nanocomposite. The equilibrium distance between the graphene layer and the top of the Mn_3O_4(001) surface is calculated to be 2.91 Å. The interface adhesion energy was obtained according to the following equation:

$$E_{ad} = E_{comb} - E_{graphene} - E_{Mn_3O_4(001)} \quad (1)$$

where E_{comb}, $E_{graphene}$, and $E_{Mn_3O_4(001)}$ represent the total energy of the relaxed GS–Mn_3O_4 nanocomposite, the pure graphene sheet, and the clean Mn_3O_4(001) slab, respectively. The interface binding energy is as high as −4.45 eV for the whole model interface, which indicates very high stability. To characterize the electron coupling at the GS–Mn_3O_4 interface, three-dimensional charge density difference plots were calculated by subtracting the electronic charge of the hybrid GS–Mn_3O_4 nanocomposite from those of the separate graphene layer and the Mn_3O_4(001) surface as shown in Fig. 6(b). Clearly, there is significant charge transfer from the graphene layer to the Mn_3O_4(001) surface in the ground electronic state, which considerably enhances the electronic conductivity of the whole nanocomposite. The Nyquist plots also give further evidence that the charge transfer resistance has decreased in the GS–Mn_3O_4 nanocomposite, as shown in Fig. S3†. Accordingly, this can also further elucidate the intrinsic reason why the electrochemical performance of the GS–Mn_3O_4 nanocomposite enormously surpasses that of the bare Mn_3O_4 nanoparticle sample, which is virtually an insulator.

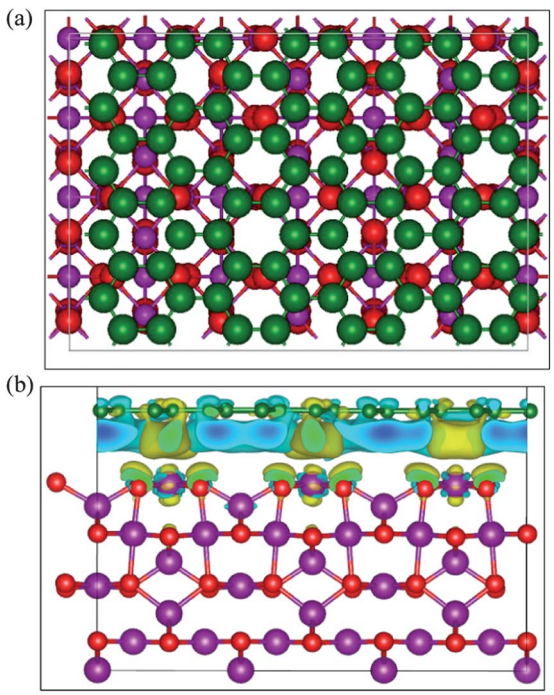

Fig. 6 (a) Top view of the optimized GS–Mn_3O_4(001) and (b) side view of a three-dimensional charge density difference plot for the interface between a graphene sheet and a Mn_3O_4(001) surface. Magenta, red, and green balls represent Mn, O, and C atoms, respectively. Cyan and yellow isosurfaces represent charge depletion and accumulation in the space, with an isovalue of 0.015 e $Å^{-3}$.

4 Conclusions

We successfully synthesized a Mn_3O_4-embedded graphene sheet nanocomposite that was directly prepared from GO *via* a facile, effective, energy-saving, and scalable microwave hydrothermal technique. The Mn_3O_4 particles in the nanocomposite, directly growing on the surface of the graphene sheets, interact with each other intimately, so that the nanocomposite exhibits better electrochemical properties than the bare sample, including a high reversible specific capacity of more than 900 mA h g^{-1} at 40 mA g^{-1}. Even at a high current density of 1000 mA g^{-1}, this material still can achieve an acceptable capacity of 400 mA h g^{-1}. In addition, the most attractive property of this nanocomposite should be its extraordinary cycling stability, with no decay in capacity for up to 50 cycles. The theoretical calculations further give evidence that there is charge transfer between the graphene and the Mn_3O_4 nanoparticles. The GS–Mn_3O_4 nanocomposite fabricated by such an energy-saving microwave hydrothermal technique could be considered as a candidate anode material in future larger scale energy storage devices.

Acknowledgements

This work was funded by an Australian Research Council (ARC) Discovery Project (DP1094261). The authors would like to thank Dr Tania Silver at the University of Wollongong for critical reading of the manuscript and Mr Darren Attard for his great contribution.

Notes and references

1 T. Yamashita and A. Vannice, *J. Catal.*, 1996, **161**, 254.
2 H. Einaga and S. Futamura, *J. Catal.*, 2004, **227**, 304.

3 M. Johns, P. Landon, T. Alderson and G. J. Hutchings, *Chem. Commun.*, 2001, 2454.
4 (*a*) N. Sakai, Y. Ebina, K. Takada and T. Sasaki, *J. Electrochem. Soc.*, 2005, **12**, E384; (*b*) W. Xao, J. S. Chen and X. W. (David) Lou, *CrystEngComm*, 2011, **13**, 5685.
5 C. C. Hu, Y. T. Wu and K. H. Chang, *Chem. Mater.*, 2008, **20**, 2890.
6 D. Pasero, N. Reeves and A. R. West, *J. Power Sources*, 2005, **141**, 156.
7 A. A. Balandin, S. Ghosh, W. Z. Bao, I. Calizo, D. Teweldebrhan, F. Miao and C. N. Lau, *Nano Lett.*, 2008, **8**, 902.
8 Z. S. Wu, W. C. Ren, L. B. Gao, J. P. Zhao, Z. P. Chen, B. L. Liu, D. M. Tang, B. Yu, C. B. Jiang and H. M. Cheng, *ACS Nano*, 2009, **3**, 411–417.
9 K. I. Bolotin, K. J. Sikes, Z. Jiang, M. Klima, G. Fudenberg, J. Hone, P. Kim and H. L. Stormer, *Solid State Commun.*, 2008, **146**, 351.
10 S. V. Morozov, K. S. Novoselov, M. I. Katsnelson, F. Schedin, D. C. Elias, J. A. Jaszczak and A. K. Geim, *Phys. Rev. Lett.*, 2008, **100**, 016602.
11 D. A. Dikin, S. Stankovich, E. J. Zimney, R. D. Piner, G. H. B. Dommett, G. Evmenenko, S. T. Nguyen and R. S. Ruoff, *Nature*, 2007, **448**, 457.
12 C. Lee, X. D. Wei, J. W. Kysar and J. Hone, *Science*, 2008, **321**, 385.
13 S. M. Paek, E. J. Yoo and I. Honma, *Nano Lett.*, 2009, **9**, 72.
14 D. Wang, D. Choi, J. Li, Z. Yang, Z. Nie, R. Kou, D. Hu, C. Wang, L. V. Saraf, J. Zhang, I. A. Aksay and J. Liu, *ACS Nano*, 2009, **3**, 90715; H. Wang, J. T. Robinson, G. Diankov and H. Dai, *J. Am. Chem. Soc.*, 2010, **132**, 3270.
15 G. D. Du, K. H. Seng, Z. P. Guo, J. Liu, W. X. Li, D. Z. Jia, C. Cook, Z. W. Liu and H. K. Liu, *RSC Adv.*, 2011, **1**, 690.
16 Y. C. Si and E. T. Samulski, *Chem. Mater.*, 2008, **20**, 6792.
17 C. Xu, X. Wang and J. W. Zhu, *J. Phys. Chem. C*, 2008, **112**, 19841.
18 R. Muszynski, B. Seger and P. V. Kamat, *J. Phys. Chem. C*, 2008, **112**, 5263.
19 N. A. Luechinger, E. K. Athanassiou and W. J. Stark, *Nanotechnology*, 2008, **19**, 445201.
20 H. K. He and C. Gao, *ACS Appl. Mater. Interfaces*, 2010, **2**, 320.
21 C. Xu, X. Wang, J. W. Zhu, X. J. Yang and L. Lu, *J. Mater. Chem.*, 2008, **18**, 5625.
22 Z. S. Wu, W. C. Ren, L. Wen, L. B. Gao, J. P. Zhao, Z. P. Chen, G. M. Zhou, F. Li and H. M. Cheng, *ACS Nano*, 2010, **4**, 3187.
23 X. Y. Yang, X. Y. Zhang, Y. F. Ma, Y. Huang, Y. S. Wang and Y. S. Chen, *J. Mater. Chem.*, 2009, **19**, 2710.
24 G. Williams, B. Seger and P. V. Kamat, *ACS Nano*, 2008, **2**, 1487.
25 H. L. Wang, L. F. Cui, Y. Yang, H. S. Casalongue, J. T. Robinson, Y. Y. Liang, Y. Cui and H. J. Dai, *J. Am. Chem. Soc.*, 2010, **132**, 13978.
26 Y. Hu, C. Liu, Y. Zhang, N. Ren and Y. Tang, *Microporous Mesoporous Mater.*, 2009, **119**, 306.
27 M. L. Dos Santos, R. C. Lima, C. Riccardi, R. Tranquilin, P. Bueno, J. Varela and E. Longo, *Mater. Lett.*, 2008, **62**, 4509.
28 X. H. Zhu, J. Y. Wang, Z. H. Zhang, J. M. Zhu, S. H. Zhou, Z. G. Liu and N. B. Ming, *J. Am. Ceram. Soc.*, 2008, **91**, 2683.
29 K. H. Seng, Z. P. Guo, Z. X. Chen and H. K. Liu, *Adv. Sci. Lett.*, 2011, **4**, 18.
30 B. J. Li, H. Q. Cao, J. Shao, M. Z. Qu and J. H. Warner, *J. Mater. Chem.*, 2011, **21**, 5069.
31 T. Cassagneau, J. H. Fendler, S. A. Johnson and T. E. Mallouk, *Adv. Mater.*, 2000, **12**, 1363.
32 Y. G. Wang and H. S. Zhou, *Energy Environ. Sci.*, 2011, **4**, 1704.
33 A. Gupta, G. Chen, P. Joshi, S. Tadigadapa and P. C. Eklud, *Nano Lett.*, 2006, **6**, 2667–2673.
34 M. C. Bernard, A. Hugot-Le Goff, B. V. Thi and S. Cordoba de Torresi, *J. Electrochem. Soc.*, 1993, **140**, 3065.
35 C. M. Julien, M. Massot and C. Poinsignon, *Spectrochim. Acta, Part A*, 2004, **60**, 689.
36 P. Poizot, S. Laruelle, S. Grugeon, L. Dupont and J. M. Tarascon, *Nature*, 2000, **407**, 496.
37 D. Pasero, N. Reeves and A. R. West, *J. Power Sources*, 2005, **141**, 156.
38 S. Grugeon, S. Laruelle, L. Dupont and J. M. Tarascon, *Solid State Sci.*, 2003, **5**, 895.
39 S. Laruelle, S. Grugeon, P. Poizot, M. Dolle, L. Dupont and J. M. Tarascon, *J. Electrochem. Soc.*, 2002, **149**, A627.
40 J. S. Do and C. H. Weng, *J. Power Sources*, 2005, **146**, 482.